Components of the spatially-averaged turbulent stress in open channel flows over rough beds

D. Pokrajac
School *of Engineering, University of Aberdeen, Aberdeen, UK*

C. Manes
Politecnico di Torino, Dipartimento di Idraulica, Trasporti edy, Torino, Italy

ABSTRACT: We investigate spatially heterogeneous open channel flows over rough beds using double averaging methodology. This methodology is based on averaging the fundamental flow equations twice, once in time and once in space. The resulting double-averaged equations can be used as a framework for development of turbulence models. In order to fully explore the potential of such models the stress terms that appear in the momentum equation as a result of each averaging step need to be parameterised. We investigate the stress terms resulting from the double-decomposition of instantaneous velocity. The experimental values of these stress terms were determined from the laboratory experiments involving Particle Image Velocimetry (PIV) measurements of shallow open channel flows over rough beds. The structure of the stress terms and associated turbulent events is investigated using quadrant analysis. For this purpose quadrant analysis is applied either to large-scale or to small-scale velocity fluctuations. The former reveals predominant directions of large turbulent events i.e. of the motion of fluid lumps of size comparable to flow depth. The latter shows the features of small-scale turbulence. The analysis was performed for open channel flows over two types of rough beds: square bars at different spacings and uniform size spheres. It showed that large-scale turbulence in rough wall boundary layers is more anisotropic than the small-scale turbulence. This is a well-known feature, which provides the basis for LES turbulence modelling.

Keywords: Double-averaging, Rough-bed turbulent flows, Turbulent shear stress, LES

1 INTRODUCTION

The majority of natural open channel flows are fully developed turbulent flows over rough beds. In the vicinity of a rough bed, flow is always spatially heterogeneous, so it is difficult to interpret experimental results because they depend on the position of the observation point. This difficulty can be overcome by sampling data from a large number of points (sufficient to provide statistically representative sample) and by subsequently interpreting the data using the double-averaging methodology.

The double-averaging methodology is based on averaging fundamental equations twice, once in time (or over an ensemble) and once in space. The theory of spatial averaging was first developed for general conservation equations in multiphase systems in porous media flows (Whitaker 1967, Whitaker 1973, Gray 1975, Hassanizadeh and Gray 1979 etc.). The idea of applying spatial av-

eraging to time-averaged flow equations was gradually developed through the contributions of Smith and McLean (1977), Wilson and Shaw (1977), Raupach and Shaw (1982), Finnigan (1985), Raupach et al. (1991), Wang and Tackle (1994), Gimenez-Curto and Corniero Lera (1996), etc. Application of the double-averaging methodology to open channel flows over rough surfaces began only recently (Nikora et al. 2001, 2007).

For fixed bed geometry, either order of averaging steps (i.e. first time, then space and first space, then time) produces identical results. In order to prove this, Pedras, de Lemos (2001) proposed the double decomposition of flow velocity, which results in splitting both mean velocity and turbulent velocity fluctuation, into spatial average and spatial perturbation (disturbance), producing, altogether, four velocity components.

By using the double decomposition of instantaneous flow velocity at a point, it is

possible to decompose double-averaged momentum flux into four components. One of them is the momentum flux that remains resolved at large scale, whereas other three components can be interpreted as apparent stress terms. Two of these stress terms are defined in terms of turbulent velocity fluctuations: one contains their spatial averages and another one contains their spatial disturbances. It can be shown that adding these two components yields spatially-averaged turbulent stress. Pokrajac et al. (2008) termed them "large-scale" and "small-scale" 'small-scale' component of the spatially averaged turbulent stress, and presented the first literature data on experimental values of these stress components.

This paper presents further analysis of large-scale and small-scale turbulent velocity fluctuations and associated stress terms, based on laboratory experimental data on open channel flows over rough beds. Section 2 gives the definitions of the main concepts including double-decomposition of flow velocity and the resulting terms composing large-scale momentum flux. Section 3 presents a brief overview of the experimental procedures. Results and discussion are presented in Section 4. Besides conventional velocity profiles the results contain the profiles of large-scale and small-scale shear stress, as well as the quadrant analysis applied separately to large-scale and small-scale velocity fluctuations. These results provide insight into large-scale and small-scale turbulence in rough wall boundary layers, which are summarized in Section 5.

2 COMPONENTS OF THE SPATIALLY AVERAGED TURBULENT STRESS

Only uniform (in spatially-averaged properties) flows are considered. Time-averaging is performed over a very long time, while space-averaging is performed over a volume of fluid which is sufficiently large to capture representative samples of flow variables, and sufficiently small to be unaffected by large-scale heterogeneities. Spatial and temporal averages are denoted with square brackets and straight over-bar, respectively, while deviations from the spatial and temporal average are denoted with the wavy over-bar and prime, respectively.

A right-handed coordinate system is used throughout the paper, with (x,y,z) and (u,v,w) the streamwise, spanwise and bed-normal coordinates and corresponding velocity components, respectively. For simplicity only u and w velocities, and the associated component of turbulent shear stress are considered. Analogous analysis can be done with u versus v and v versus w.

2.1 Double-decomposition of instantaneous velocity

Primary decomposition of any flow variable, for instance streamwise velocity, is defined as

$$u = \bar{u} + u', \tag{1}$$

based on time averaging, and

$$u = \langle u \rangle + \tilde{u}, \tag{2}$$

based on spatial averaging.

Each of the primary components is subsequently decomposed once more. Expressing the r.h.s. of (1) in terms of spatial averages yields

$$u = \underbrace{\langle \bar{u} \rangle + \tilde{\bar{u}}}_{\bar{u}} + \underbrace{\langle u' \rangle + \tilde{u}'}_{u'}. \tag{3}$$

Alternatively, the r.h.s. of (2) is expressed using time averages as

$$u = \underbrace{\overline{\langle u \rangle} + \langle u \rangle'}_{\langle u \rangle} + \underbrace{\bar{\tilde{u}} + \tilde{u}'}_{\tilde{u}} \tag{4}$$

Pedras and de Lemos (2001) showed that all averaging and the deviation operators commute, e.g.

$$\langle \bar{u} \rangle = \overline{\langle u \rangle}, \quad \tilde{\bar{u}} = \bar{\tilde{u}}, \quad \langle u' \rangle = \langle u \rangle',$$

so it is easily established that the right hand side terms of (3) and (4) are identical. These terms represent components of instantaneous velocity at a point. In order of appearance on the r.h.s. of (3) these components are: the double-averaged velocity, the spatial perturbation in time-averaged velocity, spatially averaged velocity fluctuation and the spatial disturbance in velocity fluctuation.

2.2 Momentum flux terms resulting from two averaging steps

Momentum flux term in the Navier-Stokes equation contains products of velocity components. According to the well-known rule of product, each averaging step applied to this term produces an additional term. In case of averaging first in time and then in space this yields :

$$\langle \overline{u\,w} \rangle = \langle \bar{u}\,\bar{w} \rangle + \langle \overline{u'w'} \rangle =$$

$$= \underbrace{\langle \bar{u} \rangle \langle \bar{w} \rangle + \langle \tilde{\bar{u}}\,\tilde{\bar{w}} \rangle}_{\langle \bar{u}\,\bar{w} \rangle} + \underbrace{\langle u' \rangle \langle w' \rangle + \langle \tilde{u}'\,\tilde{w}' \rangle}_{\langle \overline{u'w'} \rangle} \tag{5}$$

where the second term of the middle equation had time and spatial averaging operators swapped before it was decomposed. It is easy to show that the

result on the right hand side can also be obtained with the reverse order of averaging steps, i.e. first in space and then in time.
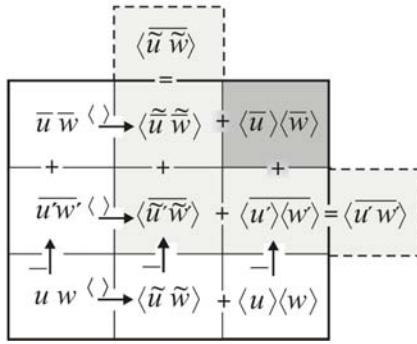

Figure 1. A matrix of terms appearing in temporal and spatial averaging.

Both procedures (i.e. time/space and space/time averaging) are summarised in Figure 1. The bottom left cell contains the starting point, namely instantaneous momentum flux at a point, uw. Temporal averaging is performed along the columns, from the bottom up and is denoted with an upwards pointing arrow with an overbar. It always produces two terms: the average of the product of fluctuations (i.e. turbulent stress term) and the product of time averages. Spatial-averaging is performed from left to right along the rows and is denoted with a horizontal arrow below square brackets. It produces the average of the product of spatial deviations (i.e. in LES terminology sub-grid stress), and the product of the spatial averages. The results of a single averaging step are shown in the left column for time averaging and the bottom row for spatial averaging. Each of these terms is then subsequently averaged once more to produce two components. Either way, the two averaging steps produce the four terms in the grey cells of Figure 1. Among them the term in the top right cell (dark grey) contains the double-averaged velocities so it represents resolved momentum flux (at large scale), whereas the sum of the other three terms (light grey cells), can be considered apparent stress term, i.e.

$$\frac{\tau_{app}}{\rho} = -\langle u' \rangle \langle w' \rangle - \langle \tilde{u}' \tilde{w}' \rangle - \langle \tilde{\bar{u}} \; \tilde{\bar{w}} \rangle . \qquad (6)$$

The first two terms on the r.h.s. of (6) are the large-scale and the small-scale turbulent stress, respectively. As indicated in Figure 1, added together they yield the spatially-averaged turbulent stress (the top cell in Figure 1). The third term on the r.h.s. of (6) is the form-induced stress. Adding this term to the small-scale turbulent stress results in time-averaged sub-grid stress (shown in the right hand side cell in Figure 1). The form-induced stress has so far received a reasonable attention in the literature. In contrast, other two

terms, i.e. the large-scale and small-scale components of the spatially-averaged turbulent stress have been almost completely neglected so far. The remaining part of the paper explores these components using experimental data on shallow open channel flows over rough beds.

3 EXPERIMENTAL METHODOLOGY

In the following text we provide a brief summary of the methodology and procedures used for the experiments presented in this paper. A more detailed description can be found in Pokrajac et al. (2008) and Manes et al. (2007).

The experiments were conducted in a tilting hydraulic flume which is 11m long and has a straight rectangular, 0.4m wide cross section. At the downstream end of the flume the flow is controlled by means of six vertical vanes which can be rotated about their vertical axis to constrict the flow until it reaches uniformity. For each experiment flow uniformity was checked by measuring the flow depth at different locations with a Vernier calliper. The entire flume bed was covered with two types of roughness elements: *i)* two-dimensional square bars of size k=6.4mm and *ii)* 12mm-diameter glass marbles.

Square bars were positioned in the flume with a spacing of $\lambda = 3k, 5k, 15k$, where λ is centre-to-centre distance between the bars. This is expressed as a dimensionless variable $L=\lambda/k = 3,5,15$. According to Perry et al. (1969), these bar spacings correspond to "*d*-type", "transitional" and "*k*-type" roughness, respectively. Alternatively, according to Morris (1955) these spacings produce "skimming", "transitional", and "isolated obstacles" flow, respectively.

Glass marbles were placed in the flume to form one layer of spheres packed in a cubic pattern.

For both bed configurations flow velocities were measured by means of Particle Image Velocimetry (PIV). Hollow glass spheres with a mean diameter of 15 μm were used as the seeding material. A Nd-Yag laser with pulse energy 300 mJ was used as a light source to illuminate vertical planes positioned along the longitudinal centreline of the flume. PIV images were then captured with a digital camera synchronized with the laser and focused on a flow region covering at least one roughness wavelength in length and the whole flow depth in height. The images were then processed to work out the velocity field. The PIV set-up used for the experiments allowed to measure bed parallel and bed-normal velocities, i.e. u and w, with the sampling frequency of roughly 13Hz. The sampling volume for each velocity vector was defined by a 32×32 pixels interroga-

tion area, corresponding to the physical dimension which varied between 1.6 and 3mm. A 75% overlap between adjacent interrogation areas allowed to have high spatial resolution (0.4 to 1.5mm), required for the data analysis presented in this paper.

All experiments were performed with the bed slope 1/400. Other hydrodynamic conditions used for the experiments are summarized in Table 1

Table 1. Hydrodynamic conditions of the experiments: k = roughness height; H = flow depth measured from the roughness top to the free surface; u_* = friction velocity; U = depth-averaged velocity, Re=UH/ν is the bulk Reynolds number; Re$_k$ =$k u_*/\nu$ is the roughness Reynolds number.

Experiment	k mm	H mm	u_* m/s	U m/s	Re	Re$_k$
BARS, L=3	6.4	44	0.0300	0.310	15500	192
BARS, L=5	6.4	44	0.0316	0.232	11600	202
BARS, L=15	6.4	44	0.0332	0.207	10350	212
SPHERES	12	42	0.0300	0.340	16320	384

4 RESULTS AND DISCUSSION

All experimental results are presented with the origin of the bed-normal coordinate z located at the roughness crest.

4.1 Data processing

Each experiment resulted in a time series of u and w velocity at a matrix of points across the measurement window. Time averaging was performed over the whole duration of the experiment (around 5min.) Spatial averaging was performed over a thin bed-parallel volume, whose height was equal to the height of the PIV interrogation area. In case of square bar roughness the averaging volume was spanning over two roughness wavelengths λ for L=3 experiment, and a single wavelength for other two experiments. This means that the averaging length was similar for L=3 and L=5 experiments but much larger in L=15. Use of a short window in the L=15 experiment was not possible since it would not have produced representative averages, while longer window for the other two experiments was not available. We made an assumption that in all three cases there was enough scale separation to provide a stable result of Reynolds stress decomposition into large-scale and small-scale components. Unfortunately our data set for square bar experiments does not cover a wide enough measurement window to allow a full test of this hypothesis.

In case of spherical roughness averaging volume was spanning along two spheres.

Time series of turbulent velocity fluctuations at each measurement point, $u'(x,z)$, were subsequently averaged in space, in order to obtain the time series of large scale velocity fluctuations, $\langle u'\rangle(z)$. The time series of $\langle u'\rangle(z)$ was calculated for each averaging volume, i.e. for each bed-parallel plane located at different height z. Time series of the small-scale velocity fluctuations $\tilde{u}'(x,z)$ were subsequently obtained by subtracting $\langle u'\rangle(z)$ from $u'(x,z)$. The analogous procedure was applied for the w velocity.

The large scale component of the turbulent shear stress was obtained by averaging $\langle u'\rangle\langle w'\rangle$ over time. The small scale component was calculated by double-averaging the product $\tilde{u}'\tilde{w}'$.

4.2 Double-averaged velocity

All experiments analyzed herein involved uniform fully developed rough-bed open channel flow with the relative submergence (the ratio of flow depth, H, to the roughness height, k) of around 10. Since the top of the roughness layer may extend until several roughness heights (2-5k, Raupach et al, 1991), and the top of the logarithmic layer is expected at approximately 0.2 flow depth (i.e. around 2k for H/k=10), the flow depth in these experiments did not provide sufficient space for development of the log-layer, i.e. the roughness layer was covering the space "reserved" for the log-layer. For this reason we did not attempt to fit the velocity profiles to the log-law.

Figure 2 shows the vertical profiles of the double-averaged streamwise velocity, scaled with the u_*, for all experiments. The profiles show how different bed roughness has different efficiency in extracting momentum from the main flow: uniform size spheres are smoothest, i.e. least efficient in extracting momentum, followed by the d-type roughness (BARS, L=3) where main flow skims over the roughness elements and hence does not "feel" their height, followed by transitional (BARS, L=5), and finally k-type roughness (BARS, L=15), which is roughest, i.e. the most efficient in extracting momentum. It is interesting to note that comparing the roughness Reynolds numbers would lead to different conclusion: based on Re$_k$ spheres would appear to be the roughest bed. The reason for this is that sphere diameter, used as a nominal roughness height, does not truly represent the height of the roughness "felt" by the flow– the latter is much smaller, so the Reynolds number that truly represents how rough is the rough surface should be based on this smaller roughness height. However, taking the grain diameter as roughness height is a common practice for gravel bed rivers, so it was adopted in this paper as well.
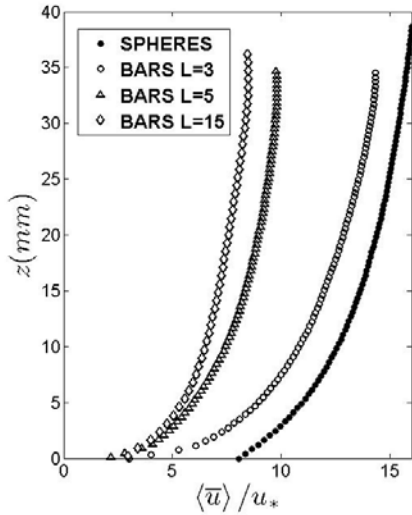
Figure 2. Double-averaged velocity profiles.

4.3 *Spatially averaged turbulent shear stress*

Figures 3 and 4 show the vertical profiles of the large-scale and small-scale turbulent stress, as well as the sum of these two, i.e. the spatially averaged shear stress. There is a notable difference in shape between the large-scale and the small-scale shear stress profiles observed in all experiments. The large-scale stress achieves its maximum value at around 0.2-0.25 of the flow depth and this maximum is smooth. In contrast, the small-scale stress has a very distinct peak around the roughness crest. This general shape is consistent with the physical meaning of the shear stress components. Large-scale stress peaks around the middle of the flow depth, where the large turbulent structures have enough space to develop, while the small-scale stress is more predominant at the roughness crest, in the zone of intense generation of small eddies. A very sharp peak in the small-scale stress is due to the constant roughness height, which creates a distinct shearing layer at the roughness crest.

It should be pointed out that all shear stress terms result from averaging over the volume of fluid only. Below the roughness crest this volume is smaller than above, because an averaging volume contains the solid phase (roughness elements). As a result the spatially averaged momentum balance equation contains the (spatially averaged) shear stress multiplied with the ratio of the volume of fluid and the total volume = porosity ϕ (e.g. Nikora et al. 2007). This also applies to the large scale and small scale stress terms presented in this paper. In the SQUARE BAR experiments porosity has a step change at the roughness crest (just above the crest it is unity, and just below it becomes 0.67, 0.80, and 0.93, for $L=3$, $L=5$ and $L=15$ experiment, respectively). The sharp change of porosity causes a second peak of the shear stress just below the roughness crests ($z=0$, Figure 3). The lower peak is visible for experiments $L=3$, $L=5$, but not for $L=15$ where the change of porosity, compared to other two experiments, is smaller. The second peak can be explained as follows. Turbulent momentum fluxes through the planes just above and just below the roughness crest are similar. (The difference comes from the viscous shear stress across the roughness crest, which is much smaller than other terms in momentum balance). However, the corresponding bed-parallel area is considerably larger above the roughness. In order for the similar momentum flux to pass through the smaller area below the roughness crest, its magnitude has to increase. Indeed, when the stress terms are multiplied with the appropriate porosity, the lower peaks in the stress profiles disappear and the graphs monotonically decrease below the roughness crest.
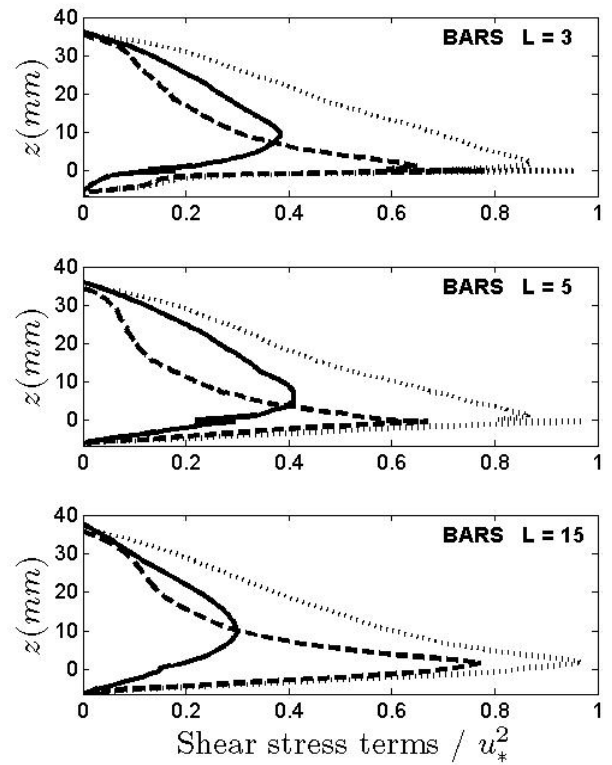

Figure 3. Profiles of: large-scale turbulent stress (full line), small-scale turbulent stress (dashed line) and the total turbulent stress (dotted line) in square bar experiments
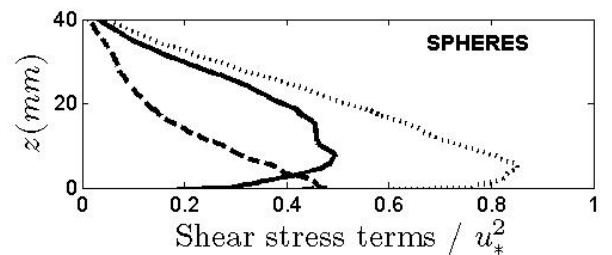

Figure 4 Profile of large-scale turbulent stress (full line), small-scale turbulent stress (dashed line) and the total turbulent stress (dotted line) in spherical roughness experiment

79

4.4 *Quadrant analysis of large scale and small scale velocity fluctuations*

The conventional quadrant method involves studying the relationship between temporal fluctuations of velocity components, *u'* and *w'*, particularly their distribution between four quadrants numbered in the counter-clockwise order, starting with Quadrant 1 where both *u'* and *w'* are positive. Correlation between *u'* and *w'* reveals the presence of turbulent coherent structures, e.g. sweep-like events belong to Q4 (*u'*>0 and *w'*<0) while the correlation between *u'*<0 and *w'*>0 (Q2) indicates ejection-like events (Lu & Willmarth 1973, Nezu & Nakagawa 1993).

In this study an analogous technique has been applied to the large-scale and small-scale velocity fluctuations. A quadrant diagram for large-scale fluctuations can be plotted for each averaging volume (bed-parallel slice), whereas a quadrant diagram for small-scale fluctuations can be plotted for each measurement point. Figures 5-8 present the quadrant diagrams for large-scale velocity fluctuations for 3 selected planes, and for small-scale velocity fluctuations at a single point within each of these planes. In square bar experiments the position of the point for the small-scale quadrant diagrams was always at 6mm (in *x* direction) from the downstream end of the bar. In the SPHERE experiment the point was in the centre between the two adjacent spheres. Small-scale diagrams are shown for just a single point in order to save space. Inevitably there is some variability in *x* direction, but the small-scale diagrams for other points are generally similar to those shown in Figures 5-8.

There is a notable difference in shape between large-scale and small-scale quadrant diagrams: the former are much less scattered and form a well-defined strip located mainly in Quadrants 2 and 4; in contrast, the small-scale diagrams form a cloud with more even coverage of all four quadrants. In other words, the small-scale turbulent flow in our experiments was more isotropic than the large-scale flow. This is another confirmation of the well-known feature of small-scale turbulence. Indeed, the concept that small-scale turbulence remains unaffected by the large-scale flow geometry, and is therefore more isotropic, is the underlying idea of the LES turbulence modelling.

Further inspection shows that the magnitudes of large-scale and small-scale fluctuations of the streamwise velocity are similar, whereas the bed-normal fluctuations are larger for small scale events. In other words the movement of a lump of fluid perpendicular to the main flow direction is faster when the lump is small.
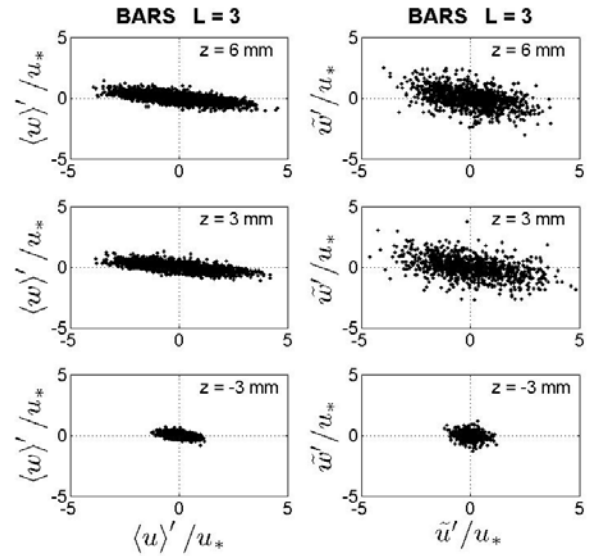
Figure 5. Quadrant diagrams of: large-scale velocity fluctuations for 3 different bed-parallel planes (left panels); small-scale velocity fluctuations at selected points in the same planes (right); for the SQUARE BARS experiment with *L*=3
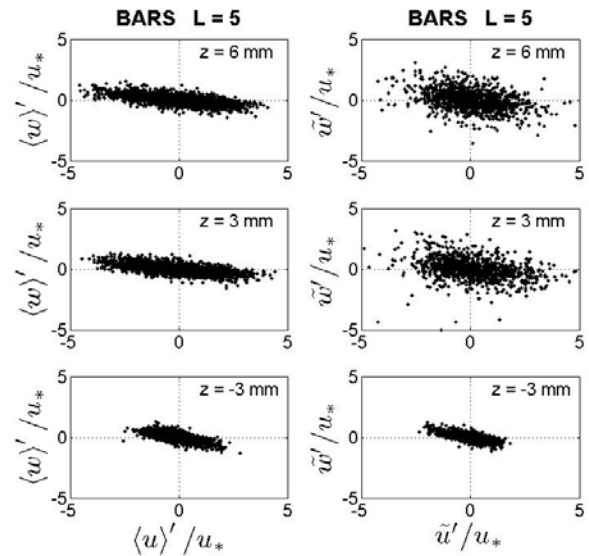
Figure 6. Same as Figure 5 for the SQUARE BARS experiment with *L*=5
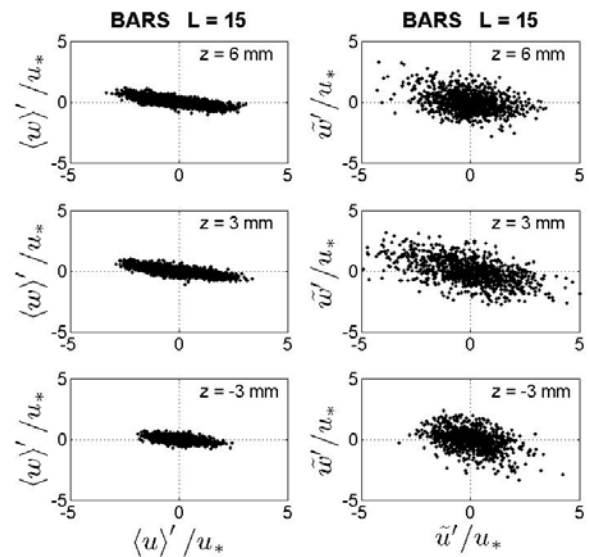
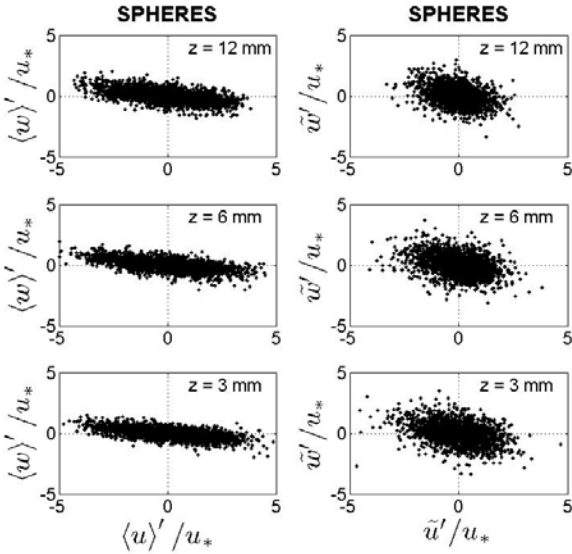Figure 7. Same as Figure 5 for the SQUARE BARS experiment with *L*=15

Figure 8. Same as Figure 5 for the SPHERES experiment.

Comparison of the quadrant diagrams for three different spacings of square bars (Figures 5-7) shows that above the roughness crest there is very little difference. Below the crest (z=-3mm), however, there is a clear difference between:

- L=3, skimming flow, where the gap between the bars contains a stable stationary vortex which suppresses turbulence generated at the roughness crest,
- L=15, flow over isolated obstacles, where the vortex behind the bar is much less stable because the re-attachment points fluctuates back and forth, and
- L=5, the transitional flow with the features between the former two.

The overall features of both large-scale and small-scale quadrant diagrams for SQUARE BARS experiments are similar to those for the SPHERES experiment. The latter experiment had somewhat wider range of large-scale w fluctuations, and somewhat more rounded shape of the small-scale quadrant diagrams. Both features are probably due to the shape and size of vertical gaps between the spheres: these gaps have longer vertical than horizontal length, whereas the gaps between the square bars are elongated in the x direction, even for L=3. The gaps between the spheres are therefore likely to enhance bed-normal velocity fluctuations and result in more rounded quadrant diagrams, especially for the small-scale turbulent motions.

All features of the quadrant diagrams presented in this section are consistent with their physical meaning, which was first discussed in Pokrajac et al. (2008).

5 CONCLUSIONS

We applied double-averaging methodology to study open channel flows over rough beds with regular geometry. In particular we investigated large-scale and small-scale velocity fluctuations, and the corresponding large-scale and small-scale turbulent shear stress.

Laboratory experiments involved fully developed turbulent open channel flows over two types of roughness: square bars at different spacings and uniform size spheres. PIV was used to obtain time series of instantaneous velocities at a large number of points across the measurement window (a vertical rectangle along the longitudinal centreline of the flume). These measurements were used to calculate large-scale and small-scale velocity fluctuations and shear stress terms. The structure of the shear stress terms was further investigated using quadrant analysis.

The following conclusions were drawn from this study:

- Double-averaging is very convenient for studying spatially heterogeneous flows such as flows over rough boundaries.
- Decomposition of turbulent velocity and shear stress into large-scale and small-scale components offers new possibilities for studying heterogeneous turbulent flows: conventional analysis of velocity statistics and other methods such as quadrant analysis can now be applied to large-scale and small-scale turbulent motions separately. This methodology has a potential to provide new insights into the structure of spatially heterogeneous flows.
- In our experiments small-scale turbulent stress always had a very sharp maximum at the level of the roughness crest, whereas large-scale turbulent stress profile was more gradual, with a maximum around 0.2 of the flow depth.
- Quadrant analysis confirmed that small-scale turbulent flow in rough bed boundary layers is more isotropic and has relatively higher bed-normal velocity than the large-scale flow. Furthermore bed-normal velocity was enhanced when the gaps between the roughness elements had a significant bed-normal length, compared to the streamwise length.

These conclusions apply solely to rough beds with regular geometry. Further research is required to establish to what extent they can be extrapolated to irregular beds of natural streams.

REFERENCES

Finnigan, J.J. 1985. Turbulent transport in flexible plant canopies. In: The forest-atmosphere interactions, B.A. Hutchinson and B.B. Hicks, eds., D. Reidel Publishing Company, 443-480.

Gimenez-Curt, L.A., Corniero Lera, M.A. 1996. Oscillating turbulent flow over very rough surfaces. Jour. Geophys. Res 101(C9), 20,745-20,758.

Gray, W.G. 1975. A derivation of the equation for multi-phase transport. Chemical Engineering Science, 30, 229-233.

Hasanizadeh, M., Gray, W,G, 1979. General conservation equations for multi-phase systems: 1. Averaging procedure. Adv. Wat. Resour. 2, 131-144.

Lu, S.S., Willmarth, W.W. 1973. Measurements of the structure of the Reynolds stress in a turbulent boundary layer. J. Fluid Mech. 60, 481-511.

Manes, C., Pokrajac, D., McEwan, I. 2007. Double-averaged open channel flows with small relative submergence. ASCE Journal of Hydraulic Engineering 133(8): 896-904.

Morris, H.M. 1955. Flow in rough conduits. ASCE Transactions 120, Paper No. 2745, 373-410.

Nezu, I., Nakagawa, H. 1993. Turbulence in Open-Channel Flows. Balkema, Rotterdam, The Netherlands.

Nikora V, Goring D, McEwan I, Griffiths G (2001) Spatially-averaged open-channel flow over rough bed. J. Hydr. Eng., 127(2), 123-133.

Nikora, V., McEwan, I., McLean, S., Coleman, S., Pokrajac, D., Walters, R. 2007. Double averaging concept for rough-bed open-channel and overland flows: Theoretical background. ASCE Journal of Hydraulic Engineering, 133(8): 873-883.

Pedras, M.H.J., de Lemos, M.J.S. 2001. Macroscopic turbulence modelling for inompressible flow through undeformable porous media. Int. Jour. Heat Mass Transfer 44, 1081-1093.

Perry, A. E., Schofield, W. H. & Joubert, P. N. 1969 Rough wall turbulent boundary layers. J. Fluid Mech. 37, 383-413.

Pokrajac, D., McEwan, I. Nikora, V. 2008. Spatially averaged turbulent stress and its partitioning. Experiments in Fluids, 45:73-83.

Raupach, M.R., Shaw, R.H. 1982. Averaging procedures for flow within vegetation canopies. Boundary Layer Meteor. 22, 79-90.

Raupach, M.R., Antonia, R.A., Rajagopalan, S. 1991. Rough-wall turbulent boundary layers. Applied Mech. Rev. 44, 1-24.

Smith, J.D., McLean, S.R. 1977. Spatially averaged flow over a wavy surface. J. Geophys. Res. 83(12), 1735-1746.

Wang H, Tackle ES (1994) Boundary-layer flow and turbulence near porous obstacles, 1. Derivation of a general equation set for a porous medium. Boundary Layer Meteor. 74, 73-88.

Whitaker, S. 1967. Diffusion and dispersion in porous media. AlChE J. 13, 420

Whitaker, S. 1973. Transport equations for multiphase systems. Chem. Engng. Sci. 28(1) 139-147.

Wilson, N.R., Shaw, R.H. 1977. A higher order closure model for canopy flow. J. Appl. Meteorology 16, 1197-1205.